Turbulent Transport of Trapped-Electron Modes in Collisionless Plasmas

Yong Xiao and Zhihong Lin

Department of Physics and Astronomy, University of California, Irvine, California 92697, USA

(Received 31 December 2008; published 19 August 2009)

Global gyrokinetic particle simulations of collisionless trapped-electron mode turbulence in toroidal plasmas find that electron heat transport exhibits a device size scaling with a gradual transition from Bohm to gyro-Bohm scaling. A comprehensive analysis of spatial and temporal scales shows that the turbulence eddies are predominantly microscopic because of zonal flow shearing, but the presence of mesoscale structures drives a nondiffusive component in the electron heat flux due to the weak nonlinear detuning of the precessional resonance that excites the linear instability.

DOI: 10.1103/PhysRevLett.103.085004 PACS numbers: 52.35.Ra, 52.30.Gz, 52.35.Qz, 52.65.−y

The anomalous heat loss in magnetic fusion plasmas is widely believed to arise from the microscopic turbulence excited by drift wave instability [1]. The understanding of and thus the ability to control ion heat transport have been drastically improved thanks to intensive studies of the ion temperature gradient (ITG) turbulence in fusion experiments, theory, and simulation. In contrast, electron heat transport is less understood, even though it is more important for burning plasmas such as ITER [2] since fusion products (energetic α particles) mostly heat the electrons. A prominent candidate for the electron heat transport in high temperature toroidal plasmas is collisionless trapped-electron mode (CTEM) [1] turbulence with a characteristic eddy size of the ion gyroradius (ρ_i). Despite a renewed interest [3–6], the nonlinear physics and transport properties of the CTEM turbulence remain poorly understood. We report here the device size scaling of the electron heat transport, as well as the underlying saturation mechanism and nondiffusive transport process from the largest ever gyrokinetic particle simulations.

The device size scaling of turbulent transport is one of the most important issues when predicting confinement properties of the large device ITER by extrapolating data from current devices. Tokamak experiments have reported both Bohm and gyro-Bohm scaling [7] for the ion heat transport, but more consistently gyro-Bohm scaling for the electron heat transport. Here, the gyro-Bohm scaling refers to a normalized heat conductivity independent of the device size, whereas it increases with the device size in the Bohm scaling [1]. First-principles turbulence simulation can provide important physical insights on the size scaling [8] and avoid the difficulties of the empirical scaling in isolating a specific type of the turbulence and in varying the device size while keeping all other dimensionless parameters fixed. Our large scale simulations of the CTEM turbulence using the global gyrokinetic toroidal code (GTC) [9] find that the electron heat transport exhibits a gradual transition from the Bohm to gyro-Bohm scaling when the device size is increased.

The deviation from the gyro-Bohm scaling could be induced by large eddies [10], turbulence spreading [8], and a nondiffusive transport process [11,12]. In our simulations, radial correlation function shows that the CTEM turbulence eddies are predominantly microscopic (a few ρ_i) but with a significant component in the mesoscale (tens of ρ_i). The macroscopic, linear streamers (hundreds of ρ_i) are mostly destroyed by the zonal flow shearing, which is found to be important in saturating the linear instability and in regulating the turbulence evolution and transport process. The mesoscale eddies form in a competing process between the breaking of the macroscopic streamers by the zonal flows and the merging of the microscopic eddies.

A comprehensive analysis of kinetic and fluid time scales finds very weak nonlinear detuning of the toroidal precessional resonance of the magnetically trapped electrons that drives the linear CTEM instability. Thus the trapped electrons behave as fluid elements in the transport process, and their ballistic radial drifts across the mesoscale eddies drive a nondiffusive component in the electron heat flux. In contrast, the ions cannot drift across the mesoscale eddies due to the parallel wave-particle decorrelation [13,14], which is not operational for trapped electrons because of the bounce averaging by the fast parallel motion. The nondiffusive electron heat flux, together with the turbulence spreading, leads to an electron heat conductivity dependent on the device size, i.e., a breaking of the gyro-Bohm scaling.

In the GTC simulations, the ion is treated by the gyrokinetic equation while the electron by the drift kinetic equation. A fluid-kinetic hybrid electron model [15] is applied to improve the numerical efficiency for the electron dynamics. The following DIII-D H-mode parameters [16] are used for the nonlinear CTEM simulation: $R_0/L_{Te} = 6.9$, $R_0/L_{Ti} = R_0/L_n = 2.2$, $T_e/T_i = 1$, $m_i/m_e = 1837$, $q = 0.58 + 1.09r/a + 1.09(r/a)^2$, where a is the minor radius of the tokamak. The circular cross section model is used in the simulation with the magnetic field defined by $B = B_0/[1 + (r/a)\cos\theta]$. Linear simulations [16] show that this case is a pure CTEM turbulence instability with a maximum linear growth rate $\gamma_{\max} = 0.25 v_i/L_n$, where $v_i = \sqrt{T_i/m_i}$ is the ion thermal speed. The field mesh for the electrostatic potential consists of 32 parallel grids and a

set of unstructured perpendicular mesh with the perpendicular grid size $\sim 0.5\rho_i$ to capture the short wavelength modes. A total of 75×10^6 spatial grids and 15×10^9 particles are used in the largest ever simulation of a device size $a = 500\rho_i$ to address the disparate spatial and temporal scales. This large simulation with a real electron-to-ion mass ratio only becomes feasible on today's most powerful supercomputers.

Transport scaling.—First we examine the electron transport scaling with the system size in the CTEM turbulence. Figure 1(a) shows that the volume-averaged trapped-electron heat conductivity χ_e varies with the system size a/ρ_i, where χ_e is defined by $q_e = \chi_e n_{\rm tr} \nabla T_e$ with $n_{\rm tr}$ the trapped-electron density and $\rho_i = v_i/\Omega_i$. The heat flux q_e is computed in the simulation through $q_e = \int d^3v(\frac{1}{2}v^2 - \frac{3}{2}T_e)\delta v_E \delta h_e$, where v is the particle velocity, δv_E is the radial component of the gyroaveraged $E \times B$ drift, and δh_e is the nonadiabatic electron distribution function. When the system size is small, $a/\rho_i < 250$, the electron heat transport clearly shows the Bohm scaling. When the system size increases, the electron heat transport gradually changes to the gyro-Bohm (GB) scaling with $\chi_e = 2.5\chi_{\rm GB}$ and $\chi_{\rm GB} = \rho_i^2 v_i/a$, similar to the ion heat transport in the ITG turbulence [8]. Detailed 2D correlation analysis shows that the turbulence eddies for different machine sizes have the same microscopic scale length with a significant component in the mesoscale which drives the electron transport away from the gyro-Bohm scaling.

To verify the simulation results, extensive studies of numerical convergence have been carried out with respect to the number of particle, grid size, and time step. In particular, the effects of particle noise [17,18] and the noise-driven transport have been carefully studied in GTC simulations using a quasilinear theory together with the measured noise spectrum [13,19]. This has now been routinely exercised as part of the numerical convergence in GTC simulations [14,20]. The noise-driven transport in the CTEM simulation for the case of $a = 500\rho_i$ is plotted as a time history in Fig. 1(b). During the whole simulation period, the noise-driven transport is shown to be less than 1% of the CTEM-driven transport for both ions and electrons. We conclude that the physics results reported here are not affected by the particle noise.

Saturation mechanism.—In order to understand the turbulence structure underlying the transport scaling, we need to study the saturation mechanism in the CTEM turbulence. Figure 2 shows the poloidal plane snapshots of the electrostatic potential after the nonlinear saturation. Zonal flows are self-consistently treated in the simulation shown in the left panel. The zonal flow shearing breaks the radially elongated eddies (streamers) into small and nearly isotropic eddies. The simulation finds that zonal flows have a substantial component in the small scale with $k_r\rho_i \sim 0.7$, which cannot be easily shielded by the linear polarization [21]. For comparison, zonal flows are artificially removed in the simulation shown in the right panel, where the radial

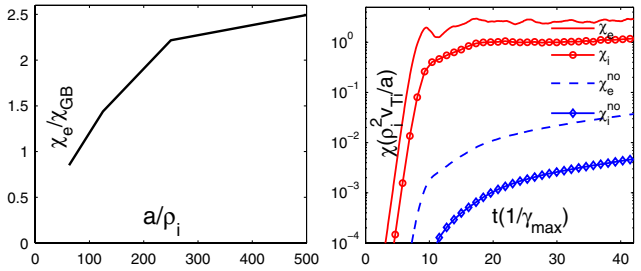

FIG. 1 (color online). The left panel (a) shows that the heat conductivity (normalized by $\chi_{\rm GB}$) of trapped electrons varies with the system size a/ρ_i. The right panel (b) shows the time history of the CTEM heat conductivity and the noise-driven heat conductivity for both ions and electrons.

streamers dominate in the saturated turbulence. The heat transport level in the right panel is 5 times larger than that in the left panel. Therefore, the zonal flow shearing is important in saturating the CTEM instability, which is confirmed by a detailed time scale analysis discussed below. Despite the shearing effects, a significant number of mesoscale eddies survive and induces a nondiffusive component on the mesoscale for the electron heat transport possibly related to the breaking of the gyro-Bohm scaling.

Transport mechanism.—To elucidate the CTEM transport mechanism, we examine the turbulence structure and various characteristic time scales for the case of $a/\rho_i = 500$. A key evidence for the transport mechanism in the ITG [8] and electron temperature gradient [20] turbulence is that the heat conductivity is proportional to the local turbulence intensity. For the CTEM turbulence, we show the time and flux-surface-averaged ion heat flux $\langle q_i \rangle$, electron heat flux $\langle q_e \rangle$, and radial $E \times B$ drift intensity $\langle \delta v_E^2 \rangle$ during the nonlinear stage in Fig. 3(d). The $\langle \delta v_E^2 \rangle$ radial profile consists of an envelope and an oscillating part with a spatial period of about $10\rho_i$. The correlation between the radial profiles of $\langle \delta v_E^2 \rangle$ and $\langle q_i \rangle$ suggests that the ion heat transport is driven by the local turbulence intensity $\langle \delta v_E^2 \rangle$. On the other hand, the radial profile of $\langle q_e \rangle$ is much smoother and lacks the small scale oscillations. Nonetheless, the global profile of $\langle q_e \rangle$ is quite similar to

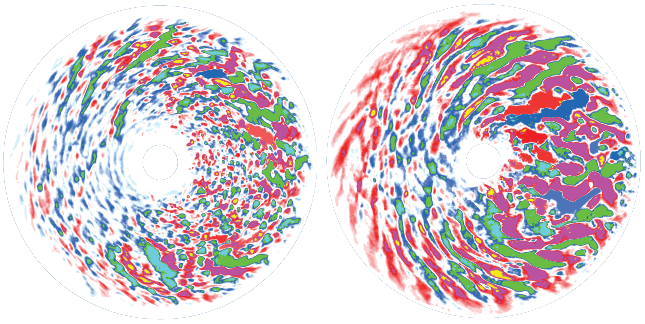

FIG. 2 (color). Poloidal plane snapshots for $a/\rho_i = 250$ case at $t = 29/\gamma_{\rm max}$. The left panel (a) shows that the zonal flows break the radial streamers. The zonal flows are artificially removed in the right panel (b) and the radial streamers dominate.

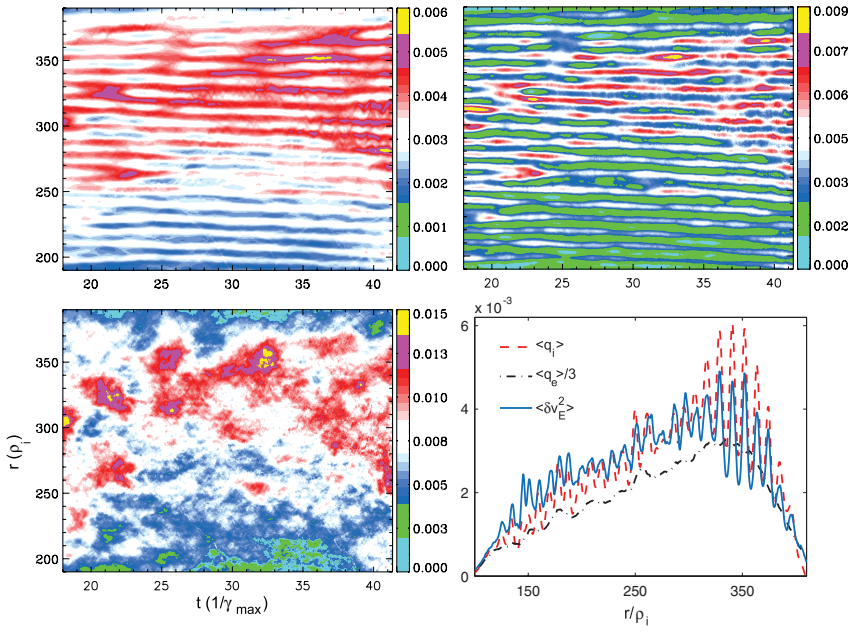

FIG. 3 (color). The time-radial contour plot is shown for ion heat flux $\langle q_i \rangle$ in the top left panel (a), turbulence intensity $\langle \delta\phi^2 \rangle$ in the top right panel (b), and electron heat flux $\langle q_e \rangle$ in the lower left panel (c). The lower right panel (d) shows the radial profiles of the time averaged $\langle q_i \rangle$, $\langle q_e \rangle$, and radial $E \times B$ drift intensity $\langle \delta v_E^2 \rangle$.

the global envelope of $\langle \delta v_E^2 \rangle$. This suggests that the electron heat transport is close to diffusive on a global scale, but not on the microscopic and mesoscales.

The radial-time contour plots of the flux-surface averaged $\langle q_i \rangle$, $\langle \delta\phi^2 \rangle$, and $\langle q_e \rangle$ are shown in Figs. 3(a)–3(c), respectively. The remarkable similarity between $\langle q_i \rangle$ and $\langle \delta\phi^2 \rangle$ in both radial structure and time evolution confirms that the ion heat transport is driven by the local fluctuation intensity. However, the electron heat flux $\langle q_e \rangle$ contains a ballistic propagation in the radial direction. This indicates that the electron heat transport may contain both diffusive and pinch terms [22]. Therefore, the electron heat transport follows the global structure of the turbulence intensity profile but contains a nondiffusive component on the mesoscale.

We define an effective decorrelation time τ_{decor}, since both ion and electron heat transport are proportional to the turbulence intensity on the global scale, i.e., $\tau_{\text{decor}} = 2D/\delta v_E^2$. Because the particle diffusivity is much smaller than the thermal conductivity as observed in the simulations, a test particle diffusivity D can be related to the electron thermal conductivity χ_e by $D = 2\chi_e/3$. It is then calculated that $\tau_{\text{decor}} = 4\chi_e/(3\langle \delta v_E \rangle^2) \approx 0.61 L_n/v_i$ for the trapped electrons. This characteristic time scale may reflect the physical process relevant to the transport mechanism [20], which could be either kinetic wave particle decorrelation or fluid eddy mixing. Through comprehensive analysis of the kinetic and fluid time scales, we can identify the physical process responsible for the transport.

The two kinetic time scales related to the CTEM eigenmodes are the wave particle decorrelation time ($\tau_\parallel$ and $\tau_\perp$) for the trapped electrons to cross the turbulence eddies in the parallel and perpendicular directions. Because of the fast bounce motion, which averages out the parallel electric field, the trapped electrons cannot decorrelate from the wave in the parallel direction, i.e., $\tau_\parallel = \infty$. In the spectral range of interest, the CTEM frequency is roughly proportional to the toroidal mode number (i.e., nondispersive). Thus the resonant electrons cannot decorrelate from the wave in the toroidal direction. Moreover, although the resonant electrons can decorrelate from the wave in the radial direction due to the radial dependence of the precessional frequency, this dependence is very weak (on the equilibrium scale). Therefore, $\tau_\perp = \infty$. The trapped electrons thus remain resonant with the wave until the eddies disappear or the electrons jump from one eddy to another, i.e., the resonant electrons behave as fluid eddies in the transport process.

To evaluate the fluid time scales, we first calculate the two-point correlation function $C_{r\zeta}(\Delta r, \Delta\zeta) = \frac{\langle \delta\phi(r+\Delta r, \zeta+\Delta\zeta)\delta\phi(r,\zeta)\rangle}{\sqrt{\langle \delta\phi^2(r+\Delta r,\zeta+\Delta\zeta)\rangle\langle \delta\phi^2(r,\zeta)\rangle}}$, where the average $\langle \ldots \rangle$ is carried out for toroidal angle $\zeta \subset [0, 2\pi]$ and radius $r \subset [150, 350]\rho_i$ at the poloidal angle $\theta = 0$. The radial correlation function $C_r(\Delta r)$ is then calculated by taking the maxima along the ridge of $C_{r\zeta}(\Delta r, \Delta\zeta)$. The function $C_r(\Delta r)$ shown in Fig. 4 clearly demonstrates a two-length-scale structure, i.e., microscopic eddies and mesoscale eddies, consistent with the contour plot in Fig. 2(a). An exponential fit of the initial drop of $C_r(\Delta r)$ gives the short length scale $L_r \approx 5\rho_i$. This is the average radial size of the microscopic eddies. The eddy turnover time $\tau_{\text{eddy}} = L_r/\langle \delta v_r \rangle$, describes how fast the eddy rotates due to the $E \times B$ drift without the zonal flow shearing. For microscopic eddies, $\tau_{\text{eddy}} \approx 1.6 L_n/v_i$. Another fluid time scale that is relevant to the dynamics of the turbulence eddies is the zonal flow shearing time, $\tau_s = [\frac{L_r}{L_\varphi}\frac{\partial}{\partial r}(\frac{qV_E}{r})]^{-1}$, which is calculated to be $\tau_s \approx 0.66 L_n/v_i$.

We now calculate the two-time-two-point correlation function $C_{t\zeta}(\Delta t, \Delta\zeta) = \frac{\langle \delta\phi(t+\Delta t,\zeta+\Delta\zeta)\delta\phi(t,\zeta)\rangle}{\sqrt{\langle \delta\phi^2(t+\Delta t,\zeta+\Delta\zeta)\rangle\langle \delta\phi^2(t,\zeta)\rangle}}$, where the potential $\delta\phi(t, \zeta)$ is recorded at $\theta = 0$ and $r = 0.5a$

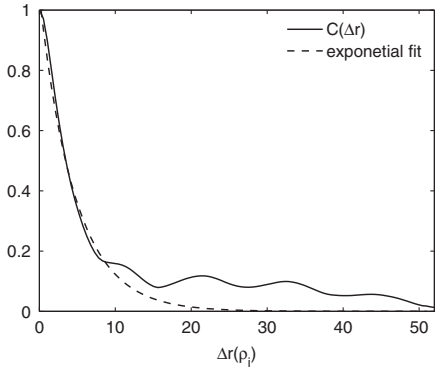

FIG. 4. The solid curve shows the radial correlation function $C_r(\Delta r)$ of the electrostatic potential as a function of the radial separation Δr. The dashed line is an exponential fit of the initial drop of $C_r(\Delta r)$.

for each time step and the average is carried out for $\zeta \subset [0, 2\pi]$ and $t \subset [20, 40]/\gamma_{\max}$. The time correlation function $C_t(\Delta t)$ is then calculated by taking the maxima along the ridge of $C_{t\zeta}(\Delta t, \Delta\zeta)$. It shows a perfect exponential decay with a decay time of $\tau_{\rm au} \approx 11 L_n/v_i$, which is the autocorrelation time of the turbulence. Therefore, this CTEM turbulence has a large Kubo number with $K = \tau_{\rm auto}/\tau_{\rm eddy} \approx 7$ for the microscopic eddies, which could affect the transport scaling [23]. Since the mesoscale eddies would have a smaller K value, the quasilinear estimate of the effective decorrelation time $\tau_{\rm decor}$ may be relevant to the transport on the global scale, which is in the transitional regime between the small and large K value.

We list all the characteristic time scales in Table I. Compared to $\tau_{\rm decor}$, the zonal flow shearing time τ_s and eddy turnover time $\tau_{\rm eddy}$ are the two closest time scales. This suggests that the decorrelation process should be mostly the eddy mixing regulated by the zonal flows. All the kinetic time scales are much larger than $\tau_{\rm decor}$, τ_s, and $\tau_{\rm eddy}$. Therefore, the electron heat transport in the CTEM turbulence is mainly a fluid process although the linear instability is driven by the kinetic process of the toroidal precessional resonance. The radially random distribution of the microscopic and mesoscale eddies enables the electrons to average out the local structure of the turbulence intensity. For comparison, we perform a simulation of the ITG turbulence with adiabatic electrons with a system size of $a/\rho_i = 500$ and also list the ITG characteristic time scales in Table I. The ion heat transport is found to be a quasilinear process [13] and regulated by the wave particle decorrelation with $\tau_\parallel = 1/\langle \Delta k_\parallel v_i \rangle$ and $\tau_\perp = 3/(4\chi_i s^2 \langle\theta^2\rangle \langle k_\theta^2 \rangle)$, using the method in Ref. [20].

Finally, the physical picture of the device size scaling of the electron heat transport in the CTEM turbulence emerges from a combination of the turbulence structure and the fluidlike nature of the electron transport process. The significant long tail of the radial correlation function in Fig. 4 indicates the existence of a large number of mesoscale eddies in Fig. 2(a). The resonant trapped electrons

TABLE I. Characteristic time scales for trapped electrons in the CTEM turbulence and for ions in the ITG turbulence.

$[L_n/v_i]$	$\tau_{\rm decor}$	$\tau_\parallel$	$\tau_\perp$	$\tau_{\rm eddy}$	$\tau_{\rm au}$	τ_s	$\frac{1}{\gamma_{\max}}$
CTEM e	0.61	∞	∞	1.6	11	0.66	4.0
ITG i	1.7	1.8	2.0	4.9	7.2	1.4	9.1

can be convected by the $E \times B$ drift across the mesoscale eddies. This mesoscale ballistic motion then drives the electron heat transport that contains a nondiffusive component on the mesoscale and smooths out the small radial structure of the turbulence intensity as shown in Fig. 3. The mesoscale ballistic electron heat flux, together with the turbulence spreading [8], leads to the deviation from the gyro-Bohm scaling for the small devices as shown in Fig. 1(a).

This work was supported by U.S. DOE SciDAC GPS-TTBP and GSEP centers. We used ORNL and NERSC supercomputers for simulations. We acknowledge S. Klasky and C. Jin for computational support, and L. Chen, P. H. Diamond, T. S. Hahm, I. Holod, and W. L. Zhang for useful discussions.

[1] W. Horton, Rev. Mod. Phys. **71**, 735 (1999).
[2] http://www.iter.org.
[3] D. Ernst *et al.*, Phys. Plasmas **11**, 2637 (2004).
[4] J. Lang, S. Parker, and Y. Chen, Phys. Plasmas **15**, 055907 (2008).
[5] F. Merz and F. Jenko, Phys. Rev. Lett. **100**, 035005 (2008).
[6] R. Waltz and C. Holland, Phys. Plasmas **15**, 122503 (2008).
[7] C. Petty *et al.*, Phys. Plasmas **9**, 128 (2002).
[8] Z. Lin, S. Ethier, T. Hahm, and W. Tang, Phys. Rev. Lett. **88**, 195004 (2002).
[9] Z. Lin *et al.*, Science **281**, 1835 (1998).
[10] F. Romanelli and F. Zonca, Phys. Fluids B **5**, 4081 (1993).
[11] P. H. Diamond and T. S. Hahm, Phys. Plasmas **2**, 3640 (1995).
[12] R. Sanchez *et al.*, Phys. Rev. Lett. **101**, 205002 (2008).
[13] I. Holod and Z. Lin, Phys. Plasmas **14**, 032306 (2007).
[14] W. Zhang, Z. Lin, and L. Chen, Phys. Rev. Lett. **101**, 095001 (2008).
[15] Z. Lin *et al.*, Plasma Phys. Controlled Fusion **49**, B163 (2007).
[16] G. Rewoldt, Z. Lin, and Y. Idomura, Comput. Phys. Commun. **177**, 775 (2007).
[17] A. Aydemir, Phys. Plasmas **1**, 822 (1994).
[18] R. Hatzky, T. Tran, A. Konies, and R. Kleiber, Phys. Plasmas **9**, 898 (2002).
[19] A. Bottino, Phys. Plasmas **14**, 010701 (2007).
[20] Z. Lin *et al.*, Phys. Rev. Lett. **99**, 265003 (2007).
[21] Y. Xiao and P. Catto, Phys. Plasmas **13**, 102311 (2006).
[22] M. Vlad, F. Spineanu, and S. Benkadda, Plasma Phys. Controlled Fusion **50**, 065007 (2008).
[23] M. Vlad *et al.*, Plasma Phys. Controlled Fusion **46**, 1051 (2004).